Preparations for Tomographic Background-Oriented Schlieren Measurements in the 11-by 11-Foot Transonic Wind Tunnel

Joshua M. Weisberger*, Brett F. Bathel†, and Stephen B. Jones‡
NASA Langley Research Center, Hampton, VA, 23666

Mark R. Woike§ and Jonathon D. Ponder¶
NASA Glenn Research Center, Cleveland, OH, 44135

James T. Heineck‖ and Edward T. Schairer**
NASA Ames Research Center, Moffett Field, CA, 94035

Efforts from a collaboration involving NASA's Langley, Glenn, and Ames Research Centers to construct and test a tomographic background-oriented schlieren system in preparation for testing at the Ames 11-by 11-foot Transonic Wind Tunnel are discussed. To prepare for the test and to evaluate the probability of success, a mock-up of the tunnel test section was constructed at Langley. Schematics and renderings of the tunnel were used to place eight gigabit Ethernet CMOS cameras circumferentially around approximately $180°$ of the mock-up. Camera modules designed in-house were used to provide on-axis lighting to get maximum intensity return from the retroreflective backgrounds. A data acquisition system was designed to control the eight cameras and light sources with an acquisition rate of 4 Hz. A novel method for creation of the speckled background was developed for the test, enabling simple application and removal of the material on the tunnel walls. A tea light candle and a heat gun with two different nozzle shape attachments were used to provide an index of refraction gradient field to assess the quality of the 2D and tomographic results from the system. The heat gun was again used as an initial test article after the camera system had been set up at the Ames tunnel, giving similar results to those seen at the mock-up, and indicating a high probability of success for the testing campaign.

I. Introduction

NON-INTRUSIVE flow visualization techniques, such as schlieren and shadowgraph, are powerful tools for evaluating flow fields in wind tunnels. These techniques have long been the standard measurements for flow field visualization due to their simplicity and high-fidelity qualitative results. For conventional schlieren techniques, high-quality mirrors or lenses are needed, which can be prohibitively expensive or simply not feasible depending on the size of the field-of-view (FOV) necessary. Additionally, conventional schlieren and shadowgraph techniques require a direct line-of-sight through the wind tunnel test section, which may not always be available. Background-oriented schlieren (BOS), initially developed in the early 2000s, is an attractive alternative [1–4]. Similar to conventional schlieren techniques, BOS is sensitive to index of refraction (and thus density) gradients. Small distortions of a background pattern from its initial reference image result in displacements of the image based on the index of refraction gradient of the flow in the region between the imaging system and the background. Because mirrors/lenses are not needed, the size of the flow field that can be viewed is typically limited only by the background size and camera resolution. Direct shadowgraph can also be used for larger-scale measurements, but is primarily a qualitative tool [5], whereas the relations that govern the distortions in a BOS system can give quantitative results [6].

---

*Research Engineer, Advanced Measurements and Data Systems Branch, AIAA Member.
†Research Engineer, Advanced Measurements and Data Systems Branch, AIAA Senior Member.
‡Research Technician, Analytical Mechanics Associates, Inc.
§Research Engineer, Optics and Photonics Branch, AIAA Senior Member.
¶Research Engineer, Optics and Photonics Branch.
‖Physical Scientist, Experimental Aero-Physics Branch.
**Aerospace Engineer, Experimental Aero-Physics Branch.

When optical access to the flow field of interest is not limited, schlieren, shadowgraph, and BOS are all simple to set up and acquire data. However, when taking data in a wind tunnel, optical access can become a limiting factor. In smaller tunnels such as the 20-Inch Mach 6 or 31-Inch Mach 10 tunnels at LaRC [7, 8], large windows allow for an unobstructed view of the entire flow field, and the view is only limited by the mirrors/lenses being used. However, for larger tunnels such as the Unitary Plan Wind Tunnels at LaRC [9] and ARC [10], while having good optical access (i.e. large windows), webbing between the windows becomes limiting for large FOV measurements [11–13], because the mirrors/lenses must be located outside the test section. To image the entire flow field, the model is moved up/down or left/right to fill in the gaps where data was initially blocked by the webbing. For BOS measurements, this limitation can be circumvented by fixing the background material to the inner wall of the tunnel test section and placing the imaging camera between the webs to allow for an unobstructed view of the flow field.

Multi-camera, time-resolved tomographic measurements were first performed by Atcheson *et al.* [14]. Many tomographic BOS studies have been published since then, investigating density objects including, but not limited to, flames/plumes [14–19], natural convection [20], turbomachinery [21], jets [17, 22–31], and shock structures [32–35]. These studies typically include analysis of the effect of $f/\#$, optical access restrictions, number of cameras, camera orientation, and camera distribution. Many of these studies were performed in the laboratory, but the implementation of tomographic BOS systems in large-scale wind tunnels has also been performed [29, 31]. While the cost of a single-camera BOS setup can be inexpensive, adding enough cameras to provide adequate views for the reconstruction can quickly become fiscally prohibitive. The availability of relatively low-cost machine vision cameras has enabled less expensive, compact BOS systems [15–17]. To increase the number of unique views from a single camera, frame-splitters [17, 36] or a quadscope [37] can be used. Recent experiments have also demonstrated a tomographic system using a single camera with a fiber bundle to acquire all the views simultaneously [18, 19].

The calculation of the 2D BOS signal from each camera is typically accomplished using either a normalized cross-correlation method [38] or an optical flow method [39–41]. Algorithms used for the reconstruction include filtered back-projection (FBP) [21, 24], the algebraic reconstruction technique (ART) [14–16, 28, 29, 31, 35, 42], and a combination of both (FBP-ART) [20, 27]. The software used for data analysis in this paper is LaVision's DaVis software, where details of the computational aspects can be found in Nicolas *et al.* [42]. Work continues in the area of the mathematical treatment of the tomographic reconstruction [43].

This paper describes the work performed by researchers at NASA's Langley Research Center (LaRC), Glenn Research Center (GRC), and Ames Research Center (ARC) in preparation for a wind tunnel test performed at ARC in the 11-by 11-foot Transonic Wind Tunnel in December 2019. The test was used to evaluate the feasibility of the tomographic BOS measurement to characterize the three-dimensional density flow field generated by a flight vehicle at Mach numbers ranging from 1.1 to 1.4. To evaluate the likelihood of success at the tunnel, a mock-up of the tunnel test section was constructed at LaRC in November 2019, where an eight camera tomographic BOS system was installed. Small camera modules and a robust data acquisition system were developed in-house to easily mount equipment in the tight spaces at the tunnel. The calibration procedure was refined, and various density objects were tested to gain confidence that the system would provide useful results during the tunnel tests.

An overview of the ARC 11-by 11-foot Transonic Wind Tunnel facility is first given in Section II.A. The camera modules and data acquisition system, including mounting options and electrical connections, are discussed in Section II.B. Section II.C details the construction of the LaRC mock-up facility including camera, window, and background placement. The process for the creating the retroreflective BOS backgrounds for both the LaRC mock-up and the ARC tunnel tests is outlined in Section II.D. The limits of camera rotation relative to the windows to mitigate back-reflections is then investigated in Section III.A, and a detailed discussion of the calibration setup and results is given in Section III.B. Both 2D and 3D BOS results are discussed for various objects including a candle and a heat gun with different nozzle attachments in Sections III.C through III.E. Lessons learned throughout the mock-up process in preparation for the ARC tunnel tests are discussed in Section III.F, and Section IV concludes.

II. Experimental Setup

The following sections describe the wind tunnel facility at ARC (Section II.A), the camera modules and data acquisition system (Section II.B), the construction of the tunnel mock-up at LaRC (Section II.C), and the procedure for creating the backgrounds used in both the LaRC mock-up and ARC tunnel testing (Section II.D). Specific vendor and manufacturer names are explicitly mentioned only to accurately describe the test hardware. The use of vendor and manufacturer names does not imply an endorsement by the U.S. Government nor does it imply that the specified

equipment is the best available.

A. NASA Ames 11-by 11-Foot Transonic Wind Tunnel

As the purpose of this effort is to develop the tomographic BOS system for its implementation at the ARC tunnel (referred to as the "tunnel" hereafter), a discussion of the tunnel itself is prudent. A schematic of the tunnel test section can be seen in Fig. 1, where the left wall is the North wall, the right wall is the South wall, the top is the ceiling, and the bottom is the floor. The view in this figure looks downstream along the centerline of the tunnel. There are many windows and portholes surrounding the test section with physical access from the surrounding plenum. The preliminary placement of cameras (with fields-of-view represented by translucent cones) and backgrounds (represented by colored panels) is visible, and the tomographic reconstruction region-of-interest (ROI) is shown with a green translucent sphere (with a black-outlined circle denoting its center). This ROI is purposely shifted to the side of the model (Lockheed 1044 N+2 low-boom supersonic airliner configuration, 19.032 inches long, 0.65% scale), which is located on the centerline of the tunnel. The cameras are labeled with numbers 1 through 8, starting from the floor centerline and proceeding clockwise around to the ceiling. The cameras that are located at the rectangular windows (1, 4, 5, 8) have flexibility in their positioning upstream/downstream, while the cameras located in the portholes (2, 3, 6, 7) have very limited movement. To ensure the highest probability of a good tomographic reconstruction, the cameras were placed such that a full 180° coverage of the test section could be achieved, limited only by the fixed window locations.
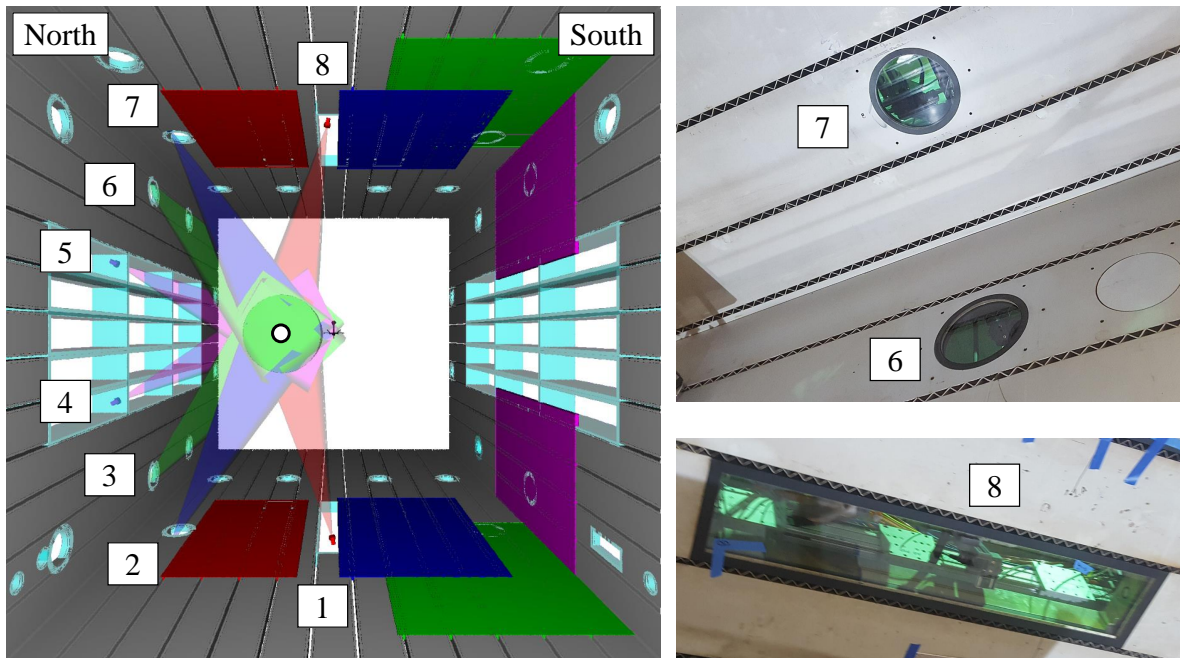

Fig. 1   Schematic of the 11-by 11-foot tunnel test section looking downstream (left), photo of portholes on North wall and ceiling (right top), and photo of rectangular window on ceiling (right bottom).

Surrounding the tunnel test section is a plenum, where during a run, equipment is exposed to reduced pressures, elevated temperatures, and increased vibrations. Installation of cameras behind the rectangular windows is relatively straightforward, with ample space and physical access. On the contrary, camera installation behind the porthole windows is difficult, with limited physical access and reduced space for rotation and translation for alignment purposes. During tunnel runs, personnel must be located in the control room, so pass-through ports are used to run any electrical connections from the plenum to the control room. Power supplies are located in the plenum.

As seen in the images in Fig. 1, streamwise baffled slots along the test section on all four walls provide a passage for air between the test section and plenum. These slots are not permitted to be covered, so backgrounds for the BOS measurements can only be placed on the solid wall panels and windows. This added a level of uncertainty to the

measurements, since the impact of the slots on the final reconstructed density fields was unknown. Data in Section III.E shows the impact these slots have on the strong refractive index gradient flow structures from a heat gun. The total pressure for all runs in the test was 2300 psf, with Mach numbers ranging from 1.1 to 1.4.

B. Camera Modules and Data Acquisition System

The camera module used for these experiments is the second iteration of the design used in Bathel *et al.* [17], and was initially designed to be a low cost, small footprint imaging system that could be used for various visualization purposes in the LaRC wind tunnel facilities (background oriented schlieren, photogrammetry, etc.). The systems were further developed for the test at ARC based on the following constraints:

1) One camera per porthole/window around half the tunnel circumference ($\approx 180°$ coverage)
2) Compact systems to fit into tight spaces in the plenum behind each window
3) Full adjustment (three axes of rotation and translation) for ideal placement to view the same ROI for all cameras
4) Low-speed acquisition (on the order of a few Hz) because time resolution is not a priority
5) Able to withstand low pressures and high temperatures in the plenum during pump-down and running
6) Short exposure to 'freeze' fluid flow up to Mach 1.4
7) Synchronously trigger all cameras remotely from control room
8) On-axis lighting to maximize intensity return from retroreflective background material
9) Minimize reflections from tunnel windows
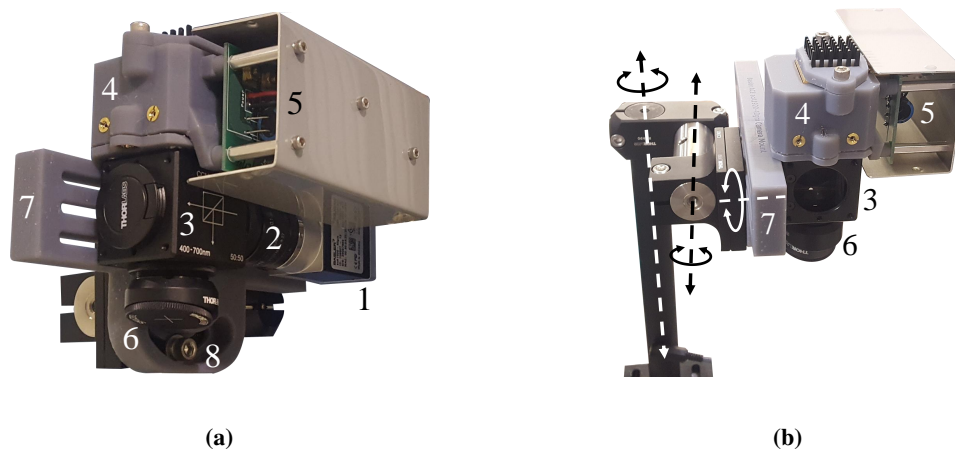10) Include an on-board PCB-based LED driver to maximize LED output intensity and minimize pulse width

(a)   (b)

Fig. 2   Single camera module (a) side view and (b) mounted to translating and rotating post structure.

A single mounted camera module can be seen in Fig. 2, which is built around a small machine vision CMOS camera (1) (Balser acA1920-40gm) with a 25 mm focal length lens (2) (Tamron, M118FM25). The lens is attached to one side of a 50/50 beamsplitter cube (3) (Thorlabs, CCM1-BS013) to couple in the on-axis lighting. On top of the beamsplitter cube is a 3D-printed housing (4) that holds a 1500 grit aspheric condenser-diffuser lens (Thorlabs, ACL2520U-DG15-A) above which an LED (CBT-120-R-C11-HK101) and heat sink are mounted. A PCB-based LED driver circuit (5) is mounted to the 3D-printed housing, with standoffs used to attach a protective covering. The LED is directly connected to the PCB with spade connectors to keep the path between the LED and the power supply as short as possible, which is important when over-driving the LEDs with high current and short pulse duration. The light from the LED is diffused by the aspheric condenser-diffuser lens in order to minimize the appearance of patterns present on the emitting surface of the LED. This lens also serves to increase the apparent size of the LED source to minimize any shadowgraph effects. This light is coupled into the viewing axis of the camera, which then reflects off the retroreflective background pattern and straight back into the camera for image acquisition. On the bottom of the beamsplitter cube is an angled neutral density filter (Thorlabs SM1L03T) and flat black cap (6) (Thorlabs SM1CP2) which are used to prevent unwanted internal reflections.

4

To connect the camera module assembly to the mounting posts, a 3D-printed adapter plate is used (7), and is fixed to the camera body and the beamsplitter cube. The Grey Pro resin (Formlabs) used for this and other 3D-printed parts was selected for its resistance to deformation at the elevated temperatures encountered inside the tunnel plenum during a run. To enable focus adjustments of the lens, the screw for the beamsplitter cube is loosened, and slides along a slot as the focus ring is adjusted. To lock the focus in place, both the focus ring set screw and the beamsplitter cube screw are tightened. The adapter plate is attached to a post mounting clamp (Thorlabs C1001), where a circular arc slot in the adapter plate allows for rotation of the entire camera module (8); the set screw is loosened, the module is rotated to the desired position, and the set screw is tightened again. The post mounting clamp and a right-angle clamp (Thorlabs RSA90) allow rotation and translation about and along the one inch post axes (dashed lines) shown in Fig. 2b.

The data acquisition equipment for the camera modules is shown in Fig. 3. Each camera (far right) has two connections: an Ethernet cable and a trigger cable. The Ethernet cable connects to a network switch (center), which is connected to a laptop (far left) for data acquisition. The Basler Pylon Viewer software is used to acquire data synchronously for all eight cameras. The trigger cables from each camera are connected to the trigger/power board (right), which acts as a central hub for all the triggering signals. The function generator (left) is also connected to the trigger board, as well as to the BNC trigger input for the LED PCB driver circuit. The function generator triggers the LEDs, controls the pulse duration of the LEDs, and controls the phase delay between the camera trigger and the LED trigger. A delay between the LED and camera trigger is needed because there is an inherent delay in the camera exposure start time after getting a trigger signal, whereas the LED response is nearly instantaneous.
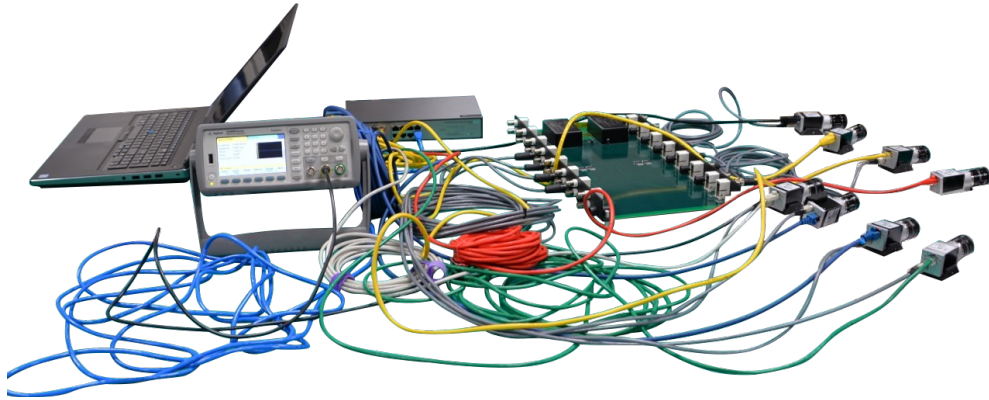

Fig. 3   Electronics used for camera module power and triggering, including laptop (far left), function generator (left), network switch (center), power/trigger board (right), and cameras (far right).

Fig. 4   All eight cameras triggering synchronously, each with an acrylic window that is used in the mock-up to simulate the ARC tunnel windows.

An image of all the camera module LEDs firing synchronously is shown in Fig. 4. A single trigger coaxial cable from the function generator is connected to camera 1 (right side of the figure), and the rest of the cameras are connected to each other with coaxial cables using BNC tee connectors. The 12 V power supplies for each camera module are shown at the bottom left of the image and power both the LED and the pulsing circuit. Individual 6 by 6 by 1/4 inch pieces of acrylic are visible in front of each camera, and are used in the LaRC mock-up to simulate the windows in the ARC tunnel.

C. Tunnel Mock-Up

The construction of the LaRC mock-up took place in November 2019, and was intended to give confidence in the performance of the system prior to traveling to ARC to set up the final system at the tunnel. The first goal was to detail a calibration method that could be applied in the limited space of the tunnel test section, and would result in a successful calibration. The second goal was to determine whether a successful tomographic reconstruction could be obtained with the camera modules placed in the same relative locations as at the tunnel facility. The limited amount of time available for setup, acquisition, and removal necessitated a "dry-run" of all the measurements prior to the actual ARC tunnel test.

Schematics and renderings of the tunnel provided by ARC were used to construct the mock-up test section and to mount camera modules in the desired locations [44, 45]. Two cameras (1 and 2) were mounted on the floor, four cameras (3, 4, 5, and 6) were mounted on the North wall, and two cameras (7 and 8) were mounted on the ceiling. Backgrounds were mounted on the floor, the South wall, and the ceiling, opposite the camera positions and based on their FOV. Due in part to the window locations at the tunnel, the cameras were not all located in the same plane, with a maximum offset between cameras in the streamwise direction (out-of-plane) of approximately 20 inches. Using the camera locations defined from the tunnel schematics and renderings, the approximate angle of the camera modules relative to the window perpendiculars was calculated: $11.1°$ for cameras 1 and 8, $31.5°$ for cameras 2 and 7, $46.3°$ for cameras 3 and 6, and $28.0°$ for cameras 4 and 5. The significance of these angles in preventing undesired reflections from the tunnel windows will be further discussed in Section III.A.

T-slot aluminum extrusions (80/20) were used to build a frame that was approximately 12-ft by 12-ft square, allowing for the camera modules to be mounted inside the frame as shown in Fig. 5. The figure only shows one half of the structure (the North wall and half the ceiling), and only includes cameras 3 through 8 (1 and 2 were installed last to avoid stepping on them). A main spine was fixed vertically on the North wall, with cameras 3 through 6 fixed to horizontally-attached beams off the spine. This allowed for the correct streamwise placement of the cameras with respect to each other (e.g. cameras 3 and 6 are further upstream than cameras 4 and 5). Cameras 7 and 8 were mounted to cross beams on the ceiling of the structure, while cameras 1 and 2 were mounted to a separate spine on the floor. The insets in Fig. 5 show zoom views of cameras 3 (blue outline) and 4 (red outline). The windows at the mock-up were aligned parallel with their respective "tunnel wall". That is, the windows in front of cameras 1, 2, 7, and 8 were horizontal, while the windows in front of cameras 3 through 6 were vertical. The windows on the floor, wall, and ceiling of the mock-up were aligned in their respective planes to approximate the tunnel wall.

After the cameras were roughly in their final positions, a plumb bob was hung from the ceiling of the structure, where the tip represented the center of the desired ROI. Note again that this ROI was purposely not located on the centerline. The tunnel wall positions were known based on the placement of the acrylic windows, and the plumb bob was positioned at the correct distance from the floor, ceiling, and wall based on the tunnel schematics/renderings. Each camera was fixed at its location in the schematic and rotated such that the plumb bob tip was at the center of its FOV. Speckled retroreflective backgrounds, discussed in more detail in Section II.D, were placed last in the mock-up. The backgrounds were fixed to the structure such that they were centered on the cameras' FOV. With the background panels in place, the cameras were focused on the background pattern and the aperture was set to $f/\# = 16$ on all cameras.

After all appropriate data sets had been acquired using a candle and a heat gun, LaVision's 2D BOS software was used to compute the 2D displacement fields from each camera view. Results from the volume calibration are discussed in Section III.B, where the position and orientation of the cameras were computed. LaVision's tomographic BOS software was then used to perform the reconstruction of the density field for qualitative evaluation, and the temperature field for quantitative comparison to a thermocouple measurement. These results are discussed in Sections III.C, III.D, and III.E.
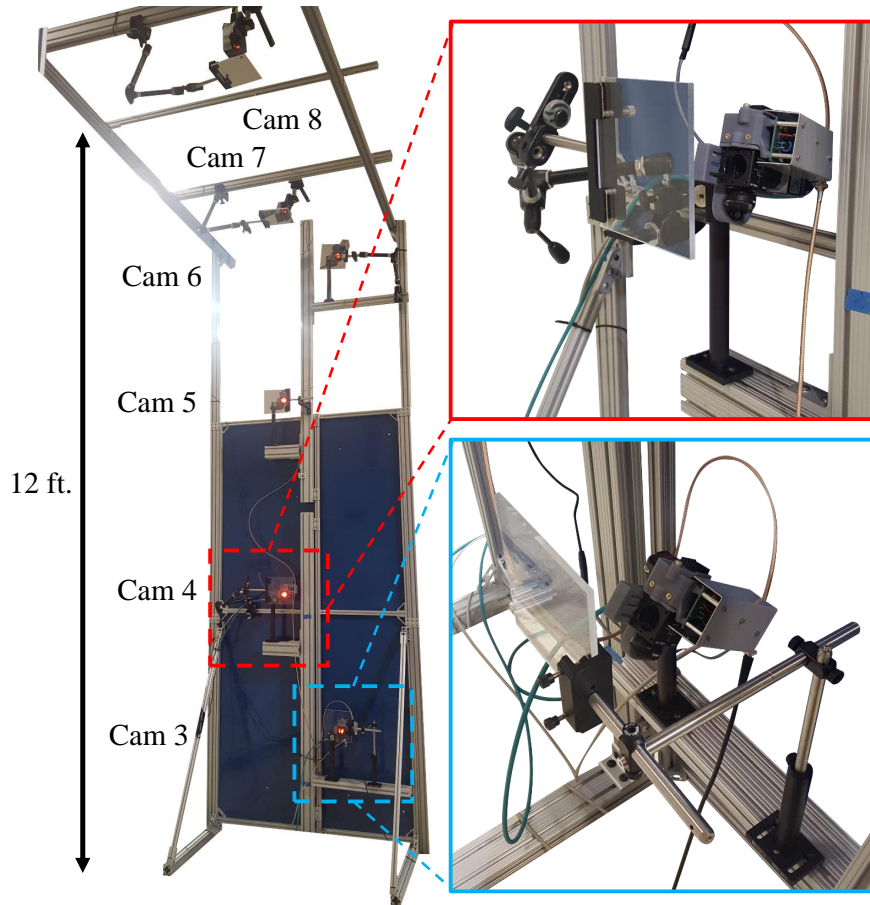
Fig. 5 **Tunnel mock-up showing six out of eight cameras installed and flashing synchronously (left), with insets showing details of cameras 3 (blue) and 4 (red).**

D. Background Material and Speckling

Constraints for the camera module operation in the tunnel plenum were discussed in Section II.B. In a similar vein, there are constraints for the background material permitted in the tunnel test section. To allow for enough coverage to obtain good 2D BOS images, the background must be located inside the tunnel, fixed to the tunnel walls and windows. A list of the constraints to be met and addressed are given below:

1) Uniform density and distribution of the retroreflective background dot pattern, based on the cameras' FOV and the distance of the cameras from the background
2) Dot pattern can be printed directly on the retroreflective background material
3) Able to be easily attached to the tunnel floor, walls, and ceiling, and remain attached during operations at supersonic Mach numbers
4) Able to be safely attached to the tunnel windows
5) Able to be removed easily without leaving any residue behind, and without removing paint from the walls
6) Retroreflective material must have high intensity return

For the mock-up testing at LaRC, items 1, 2, and 6 were satisfied. A roll of 3M Scotchlite 7610 high gain reflective sheeting was used as the retroreflective background material. Burgess *et al.* performed an analysis of the performance of this retroreflective material for photogrammetric purposes [46]. The background sizes for the mock-up were chosen to be 2 ft by 2 ft to reduce the amount of material used, and because it was not necessary to fill the entire camera FOV

for these preliminary tests. This size material does not fit through a normal printer, and it was not known whether a plot printer would be able to print the background image directly onto the material. To save time, a simplified method used a can of flat-black spray paint for the dot pattern. The nozzle of the spray paint can was enlarged from its original diameter. The background was placed on the floor, the can was held upright, and the nozzle was depressed slightly until a stream of paint particles were ejected and fell onto the background material. Pressing any harder would eject a fine mist of paint resulting in spots that were too small for the current optical setup. A combination of the enlarged nozzle diameter and the light nozzle pressure resulted in generally repeatable background patterns, but there was still variation in dot size and distribution. The sprayed backgrounds were then applied via the adhesive backing of the 7610 material to flat Alumalite panels that were cut to the appropriate size for each background. To reduce the amount of bubbles present after application, the following steps were taken, with all three persons wearing gloves to avoid depositing oil residue on the material.

1) The backing is partially peeled from one entire edge of the material by person 1, while persons 2 and 3 hold the opposite edge corners
2) The peeled edge is applied to the Alumalite panel by person 1, making sure that the edge is perfectly aligned to the edge of the panel for straight application
3) Persons 2 and 3 each hold one corner of the opposite edge with one hand, and use the other hand to hold the corners of the partially removed backing material
4) As persons 2 and 3 slowly pull on the backing material to remove it from the 7610, person 1 uses their hands to apply and smooth outward from the center, ensuring minimal bubble formation
5) Persons 2 and 3 continue to hold the 7610 material corners with one hand, applying just enough tension to keep the material from bunching as person 1 applies and smooths
6) This process continues slowly until the backing material has been completely removed, and person 1 applies and smooths the opposite edge of the material to the panel

At ARC, a method of developing a background manufacturing work flow was devised. The 7610 retroreflective sheeting was again used as the background material, since it was needed to obtain the high-intensity return mentioned earlier. This material has an adhesive backing after a shielding layer is removed, but previous experience with this material in tunnels such as the 14- by 22-Foot Subsonic Wind Tunnel at LaRC have shown that both application and removal were tedious and difficult. For application of the material to the wall of that facility, a side-panel was removed and laid flat to make the process easier, but a substantial number of bubbles were still present, requiring time to pop them before the panel could be installed again to the tunnel wall. Removal after testing was completed was also difficult, and could remove a substantial amount of the tunnel paint along with the material. To try to address these concerns, a vinyl backing (3M Wrap Film Series 1080) was applied to the 7610 material using a laminating machine. An image of
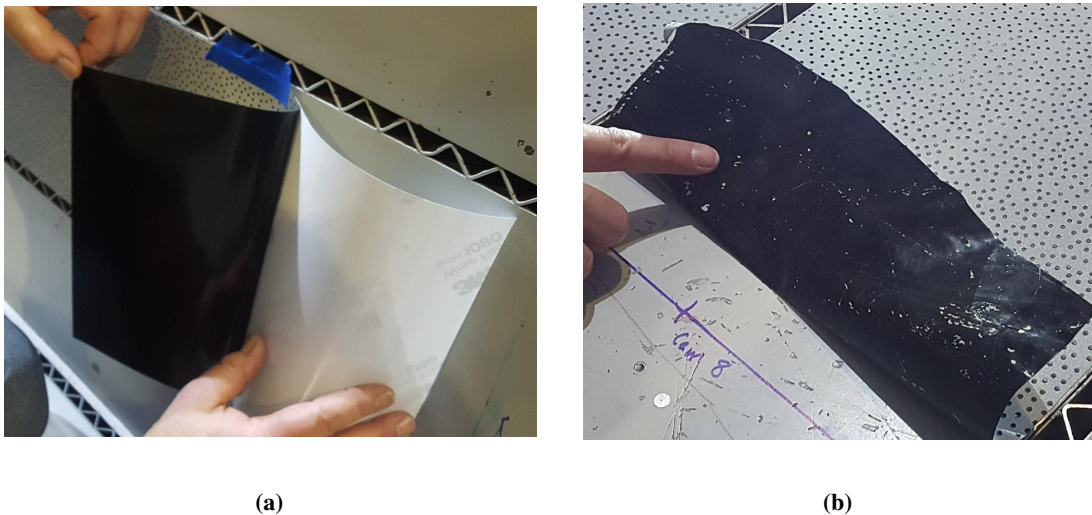

(a)   (b)

Fig. 6   Background (a) application and (b) removal at the 11-by 11-foot wind tunnel at ARC.

the protective backing removed from the vinyl material is shown in Fig. 6a during installation. Both installation and removal of this material was quick, resulting in few (if any) bubbles and negligible paint removed from the tunnel walls. The removal of the material from the ARC tunnel walls after testing can be seen in Fig. 6b, where the small white specks are the paint removed from the walls. This removal was negligible, and the paint voids seen on the wall in the figure were already present.

There is very little control over the uniformity and distribution of the spray paint method for background creation, so a more controllable method was established. The vinyl-backed 7610 material was sent to a local printing center along with a background pattern of dots designed by LaVision's speckle pattern generator software. This pattern was able to be screen printed on sheets of the 7610 material, with a resulting dot size of approximately 3 to 5 pixels when viewed by the cameras in the tunnel. The thickness of the vinyl-backing and the 7610 material are 0.119 mm and 0.127 mm, respectively. To create a smoother step at the leading edge of the material and to ensure it would not start peeling from the front during runs, aluminum tape was used to cover the leading edge, as it had proved resilient in previous testing campaigns at the ARC tunnel.

To evaluate the impact and ensure safe operation of the background material in the ARC tunnel during testing, the assembled background material was attached to the wall of a 14-inch Indraft tunnel with supersonic airfoil splitter. The impact of the edge of the material on the flow field in the tunnel as well as the integrity of the adhesion to the tunnel wall were tested. In Fig. 7, a Mach 1.2 flow was obtained at the wall, where pieces of the background were mounted, both with and without the aluminum leading edge material. In the schlieren image, shocks can be seen emanating from the wall where the background material creates a step on an otherwise flat surface. The schlieren mirror was 12 inches in diameter, and the shocks weakened significantly with increasing distance from the wall (downwards in the schlieren image).
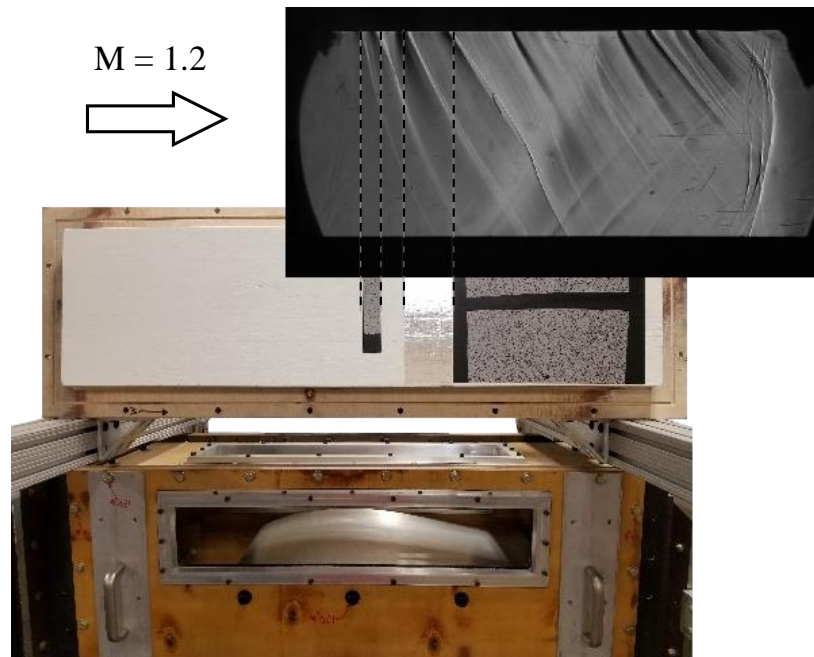

Fig. 7   Background material mounted to the top wall prior to placement in the 14-inch Indraft tunnel with supersonic airfoil splitter at ARC, and resulting schlieren image of the materials in Mach = 1.2 flow.

III. Results and Discussion

A. Camera Module Window Reflection

At the tunnel, the camera modules are placed outside the test section in the plenum, and look through the tunnel windows at their appropriate backgrounds on the opposite tunnel wall. Testing was performed at LaRC to ensure that reflections off the tunnel windows would not result in back-reflections into the camera by placing a flat piece of acrylic in front of a camera module at varying angles, from perpendicular (0°) to 10°, in 2° increments. The camera module was placed 8.75 inches from the window for the images shown in Fig. 8, which is a typical distance away from the window that a camera might be placed at the tunnel. A representative retroreflective background was placed behind the acrylic window.
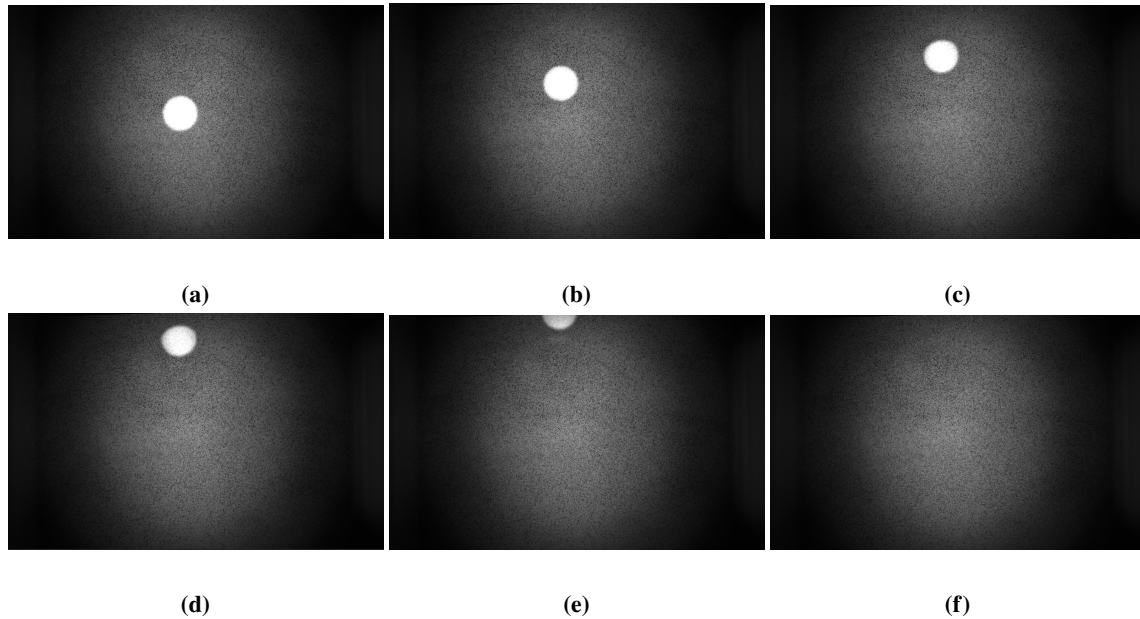

Fig. 8   Window reflections for a camera module 8.75 inches behind the acrylic window, at angles off the perpendicular to the windows of (a) 0°, **(b)** 2°, **(c)** 4°, **(d)** 6°, **(e)** 8°, **and (f)** 10°.

In each image, the full rectangular region represents the entire FOV of the camera. A diffuse bright spot with some apparent vignetting is visible in each image. This is a result of the beamsplitter cube used for the camera modules, where the aperture is too small for the camera/lens FOV. This lens/beamsplitter combination was chosen to reduce the size of the overall camera package while maintaining a larger FOV for the tunnel testing (a 50 mm lens resulted in no visible vignetting, but provided a FOV that was too small for the test). While the intensity decreases outside the main bright circle, there is still usable information in these regions. In more recent designs of the camera module system, the beamsplitter cube has been replaced with a beamsplitter plate of larger clear aperture. When using this updated design there is no vignetting, but the camera module package is larger. During the tunnel test at ARC, the FOV of the camera was reduced to a square region instead of the full rectangular region.

The bright white spot in (a) through (e) is the reflection of the diffused LED from the window back into the camera. When the camera module was rotated to 10° the reflection was no longer present, indicating that if the modules are angled at least 10° from the window perpendicular axis, back-reflections would not be a problem for the tunnel tests. When the camera modules were placed closer to the window (1.75 inches) it was seen that a minimum angle of 12° was needed. If shallower angles are needed, the camera modules can be moved farther from the windows. From the calculations in Section II.C using the expected positions of the cameras and viewing ROI, the minimum angle of the camera modules with respect to the windows was 11.1°, which is greater than the minimum angle of 10° needed to eliminate back-reflections.

B. Calibration

In the bench-top experiments performed previously in Bathel *et al.* [17], a LaVision two-level double-sided 3D calibration plate (309 mm by 309 mm) was used to obtain the volume calibration. The plate was first fixed in the center of the FOV and then translated along a single axis to provide the full volume calibration. For the LaRC mock-up, the FOV was much larger at the ROI in the tunnel (see Fig. 1), and so a larger calibration plate was needed. A single-plane calibration plate was recommended by LaVision, and a pattern design was created using the DaVis software.

(a)

(b)
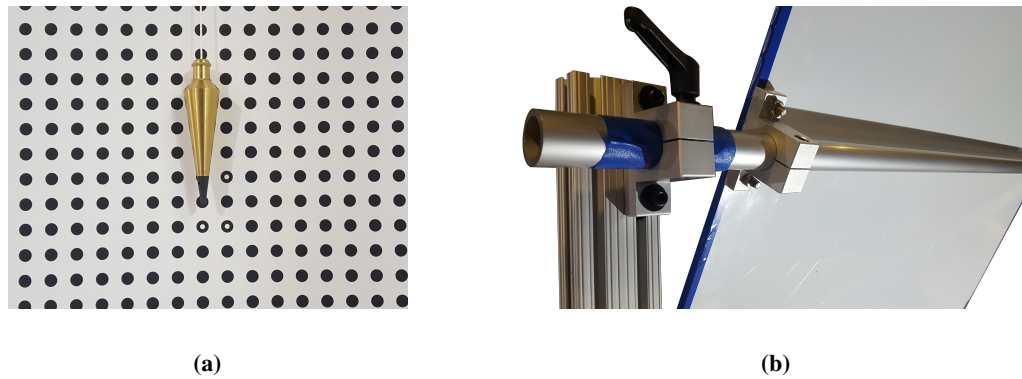
Fig. 9   Images of (a) the calibration plate and plumb bob at the center of the FOV in relation to fiducial marks, and (b) the back of the calibration plate with mounted rotation rod.
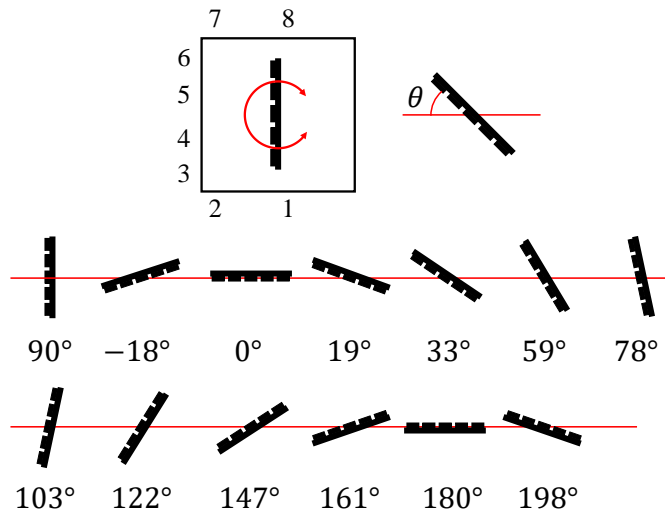
Fig. 10   Orientation of the calibration plate for 13 acquired views in the LaRC mock-up.

The calibration plate must provide sufficient coverage for all cameras when located at the model ROI. Note that the location of the plate could have been selected as the center of the tunnel, but since the origin of the tomographic reconstruction is determined by the initial view of the calibration images, the plate was placed such that its origin coincided with the ROI origin in order to more easily locate the model and flow features after the reconstruction. The dot size and spacing were 10 mm and 20 mm, respectively, with 46 dots in both the x- and y-directions. The width and height of the plate were both then 920 mm. Open circle fiducials were used to identify the coordinate axis directions and the origin of the plate. These fiducials had an offset/length in the x- and y-directions of 21/2 and 23/1, respectively. An image of a portion of the calibration plate near the origin is shown in Fig. 9a, with the plumb bob indicating the center of the ROI. From the fiducial marks, the x-axis is vertical, the y-axis is horizontal, and the z-axis is pointing out of the page.

For a board of this size (920 mm by 920 mm), a large plot printer was used to print the pattern onto a sheet of heavyweight plotter paper, which was then fixed to an Alumalite board with spray glue to ensure a flat, rigid backing for the best calibration results. This calibration plate was single-sided, and so not every camera saw the dot pattern for every image acquired during the calibration process. Each camera need not see fiducials for every image, but for each acquired image at least two cameras must be viewing the plate, and each camera should have at least three total images with the fiducials in view.

The availability of windows in the test section allowed all the cameras to be located in roughly the same plane. A round rod was fixed to the back of the calibration plate, and the rod-plate assembly permitted the plate to rotate about the rod's axis (Fig. 9b), which coincided with the tunnel streamwise axis (which is roughly orthogonal to the plane of cameras). While there are few restrictions for the images used in the calibration image set (see above discussion), the first view of the image set defines the coordinate system of the volume calibration, and thus of the reconstruction. It was decided to orient the first image of the plate at the LaRC mock-up such that it was parallel with the side-wall (North wall in Fig. 1) where cameras 3, 4, 5, and 6 are located. This places the y-axis pointing upstream, the x-axis pointing towards the ceiling, and the z-axis pointing towards the South wall. The calibration plate design used at ARC was the same, and its initial view was again chosen as parallel to the North wall. However, the plate was rotated 90° about the z-axis such that the x-axis pointed upstream, the y-axis pointed towards the ceiling, and the z-axis pointed towards the North wall.

In total, 13 distinct calibration plate positions/views were used, which can be seen in Fig. 10 with their angles noted relative to the horizontal axis. The first view of the calibration is with the plate rotated to 90°, facing the North wall (cameras 3 through 6). Images from the first view of the calibration plate in the LaRC mock-up for all eight cameras can be seen in Fig. 11. Cameras 4 (d) and 5 (e) have the most orthogonal view, while cameras 1 (a) and 8 (h) are not viewing the front of the plate because they are located behind it. In each of the views where the plate is visible, the fiducials marking the origin (open circles) are visible. From the DaVis software calibration, the de-warped calibration plate from all 13 views of all eight cameras can be seen in Fig. 12a. If the calibration fails, the de-warped image will not look like the calibration plate, so a de-warped image that has sharp fiducials over the entire plate image generally indicates a good calibration has been acquired. If the initial calibration was sub-optimal, additional views could be added to the image set, and the calibration could be run again.
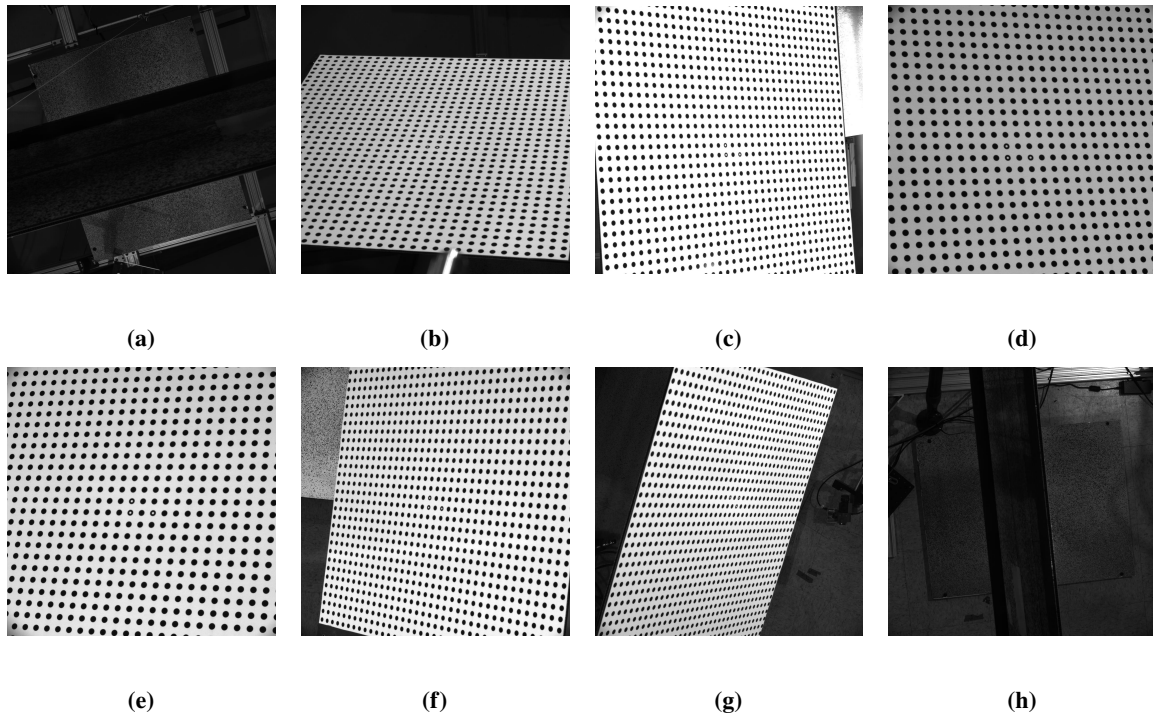

| (a) | (b) | (c) | (d) |

| (e) | (f) | (g) | (h) |

Fig. 11   First view ($\theta = 90°$) of the calibration target for cameras (a) 1 through (h) 8, which defines the origin of the coordinate system.

The calibration returns the coordinate system rotation and translation of each camera from the calibration plate
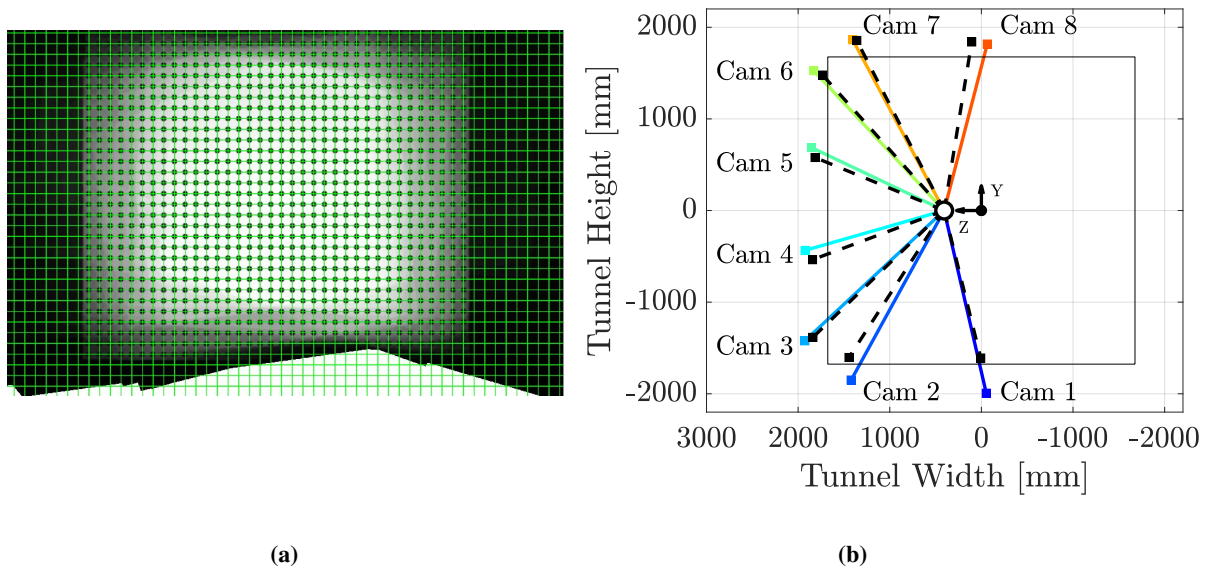
Fig. 12 (a) De-warped calibration plate image from DaVis software, and (b) camera positions of both ARC (solid colored lines) and LaRC (dashed black lines) obtained from the calibration.

origin. These values are used to plot the camera positions for both the LaRC mock-up and ARC test calibration results in Fig. 12b. The North wall is on the left, the floor is on the bottom, and the ceiling is on the top. The solid black square outline indicates the tunnel walls and the filled black circle denotes the test section centerline. The origin of the ROI is shifted off centerline as indicated in Section II.A, and is denoted with a black-outlined white circle. The y- and z-axes are labeled in accordance with the ARC tunnel calibration, and the LaRC calibration results are simply plotted in the ARC coordinate system for comparison. The camera positions of the calibration from the ARC tunnel are shown with solid colored lines, while the camera positions of the calibration from the LaRC mock-up are shown as corresponding black dashed lines. All the ARC cameras are outside the test section, located in the plenum. Cameras 1 and 2 in the mock-up appear to be inside the test section, since they were placed on the floor of the laboratory where the mock-up was built, and extended approximately 100 mm above where the tunnel floor would be. Comparing the camera positions from both calibrations, the LaRC mock-up came very close to approximating the final locations of the cameras at the ARC tunnel test. Note that there are components of the camera position in the tunnel longitudinal axis that are not shown in this view.

To compute the tomographic reconstruction, three more values were needed that were not provided directly from the calibration. The first was the distance from the calibration origin to the center of the background, which was determined using a laser range finder. The second and third values were the inclination and rotation angles of the backgrounds relative to the calibration origin. These were obtained using the relative position of the calibration plate with respect to the tunnel walls, in addition to the camera viewing angle with respect to the calibration plate (from the calibration). Images were taken for each camera with an L-square held up against their respective background to analyze the orientation of the backgrounds and compare with the results provided by the software.

C. Candle Testing

To initially test the sensitivity of the system in the LaRC mock-up to a small density object, a single tea light (candle hereafter) was used. First, all eight cameras acquired ten reference images. Then, the candle was placed on top of a rod to be held at roughly the center of the ROI. Based on the coordinate system derived from the calibration's first view, the candle was located close to the origin and the plume from the candle pointed in the positive x-direction. Ten images of the candle and plume (BOS object) were then acquired. In the laboratory mock-up, there is very little (if any) vibration that needs to be accounted for between acquisition of the reference images and the BOS object images. When running at the tunnel however, significant movement between reference images and run images was expected, and image

13

registration was required prior to computing the 2D BOS results. The work flow that was used to analyze the ARC tunnel test data was used here as well, if only to ensure all aspects of the analysis were performed the same.
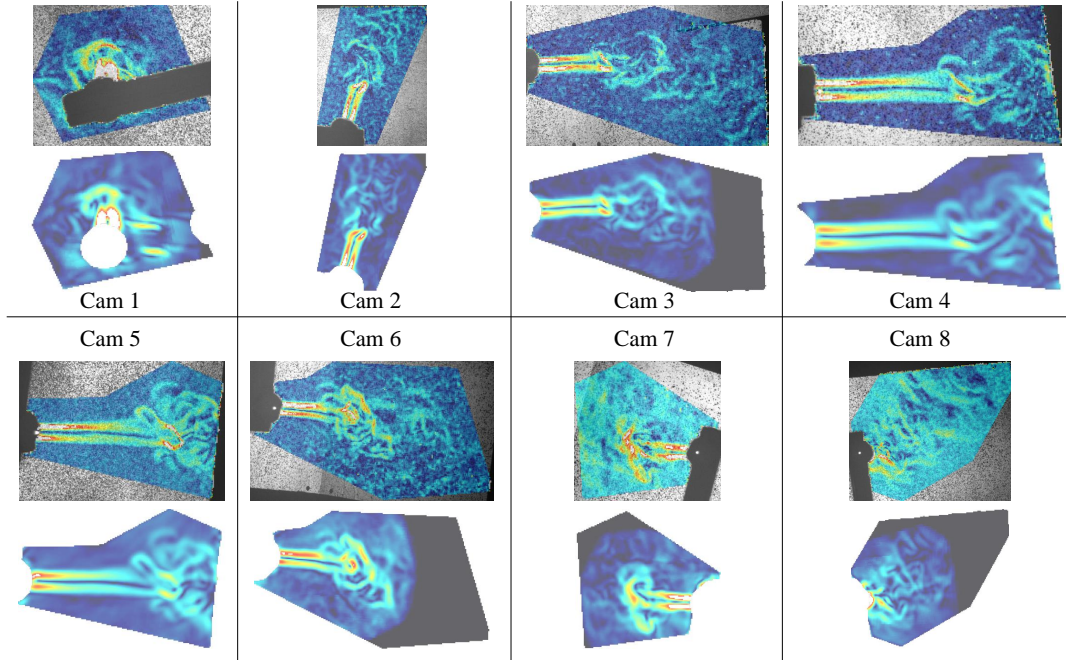

Fig. 13   LaRC mock-up single candle 2D BOS results (top image) and back-projection of the reconstruction (bottom image). Contours are colored by total pixel displacement, and have the same scale for all images.

The reference images were used to register the BOS object images. Portions of each image where no BOS signal was present were used for the registration, such as corners of the background plates (since they did not fill the entire camera FOV). At the ARC tunnel, the backgrounds filled the full camera FOV, but the baffled slots mentioned in Section II.A could be used instead. After each BOS object image was aligned to the reference images, the 2D BOS calculation was performed on the mock-up data, and can be seen in the top images for each camera in Fig. 13. Areas outside the BOS object ROI were masked out such that they were not used in the reconstruction, although this is not always necessary depending on how simple the flow field is and how little noise there is outside the BOS object region. The images shown in Fig. 13 were masked appropriately based on the extents of the plume.

Using the masked 2D BOS results and the calibration outlined in Section III.B, the tomographic reconstruction of the candle plume was computed. Using eight iso-surfaces to color the results based on temperature, the candle plume
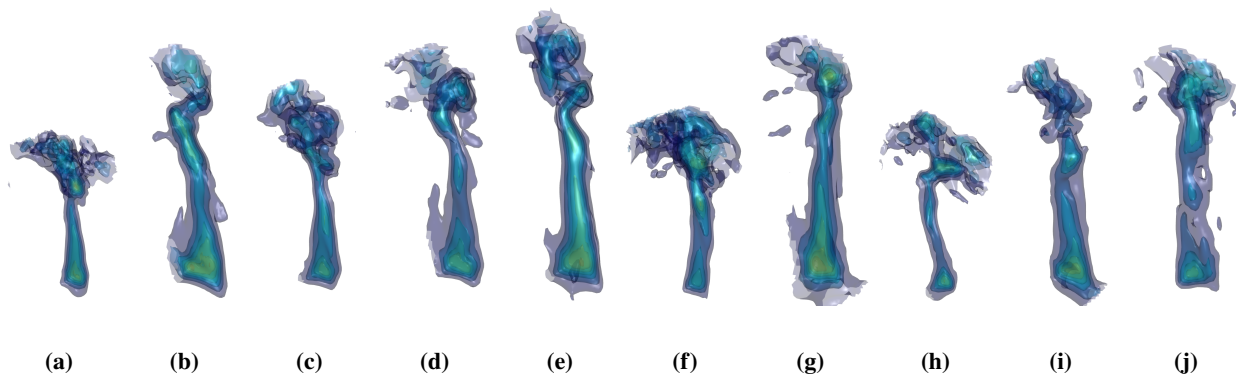

Fig. 14   Tomographic reconstruction of the candle for ten successive time frames in the LaRC mock-up, acquired at 4 Hz.

14

can be seen for all ten acquired frames in Fig. 14. The frames do not represent a time-resolved snapshot of the plume since the cameras were acquiring at 4 Hz. For time-resolved measurements, a high-speed camera setup can be used [17]. To check the validity of the tomographic reconstruction, the back-projected 2D BOS image from the reconstructed volume was viewed for each camera, and compared to the actual 2D BOS data. These comparisons can be seen in Fig. 13, where the top image for each camera is the 2D BOS data and the bottom image for each camera is the back-projection of the tomographic reconstruction of the plume. Good comparison of features between the two images gives qualitative confidence in the tomographic reconstruction of the data. A thermocouple was not used to probe the temperature of the plume in this test, but the temperatures range from room temperature up to approximately 450 K which seems low, especially down near the flame itself. The candle was placed on the rod to intentionally obscure the views of some of the cameras, and it appears that a good reconstruction was obtained in spite of the partially obscured images.

D. Round and Flat Nozzle Heat Gun

With a successful test of the candle plume, a turbulent density object was tested at the LaRC mock-up to see if the small-scale structures could be reconstructed successfully. A heat gun was used to provide a density object that would approximate the size of the model in the tunnel. First, a round nozzle was fixed to the end of the heat gun to provide a roughly axisymmetric flow. The heat gun was held such that the nozzle pointed roughly along the negative y-axis. Following the procedure used for the candle data, ten reference images for all eight cameras were first acquired, after which ten images with the heat gun on were acquired. The same image registration processing work flow was used, and the resulting 2D BOS images can be seen as the top image for each camera in Fig. 15. These 2D BOS images were then masked to retain only the signal near the plume, and the tomographic reconstruction was performed. The bottom images for each camera in Fig. 15 are again the projections of the reconstructed volume back to the appropriate camera position, and for a good reconstruction should match the actual 2D BOS images.
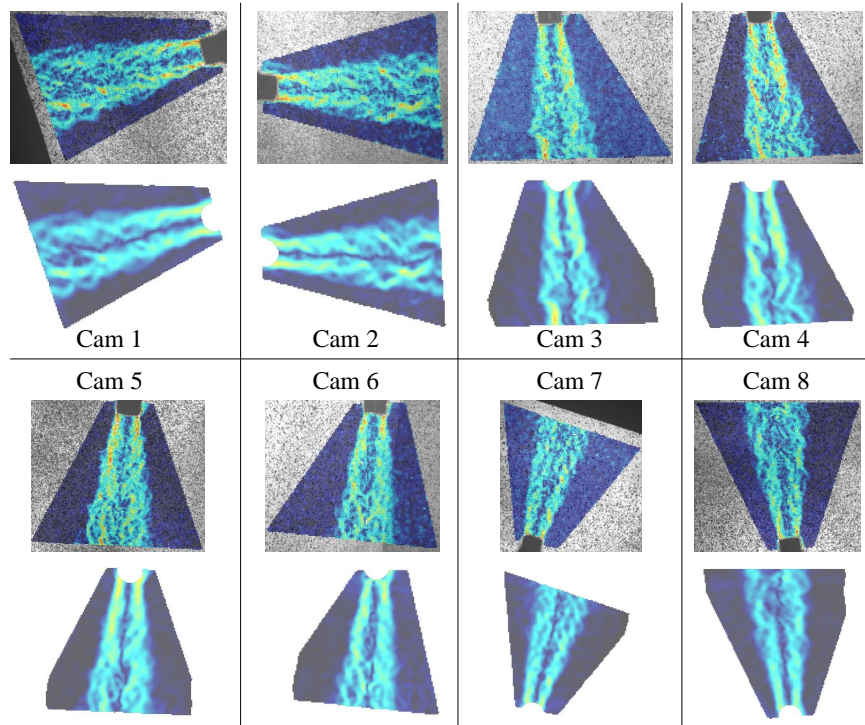

Fig. 15   Round nozzle heat gun 2D BOS results (top image) and back-projection of the reconstruction (bottom image). Contours are colored by total pixel displacement, and have the same scale for all images.

Since the round nozzle produces a roughly axisymmetric flow field, a flat nozzle was fixed to the end of the heat gun next to test the ability of the reconstruction to reproduce a fully three-dimensional flowfield. The 2D BOS results
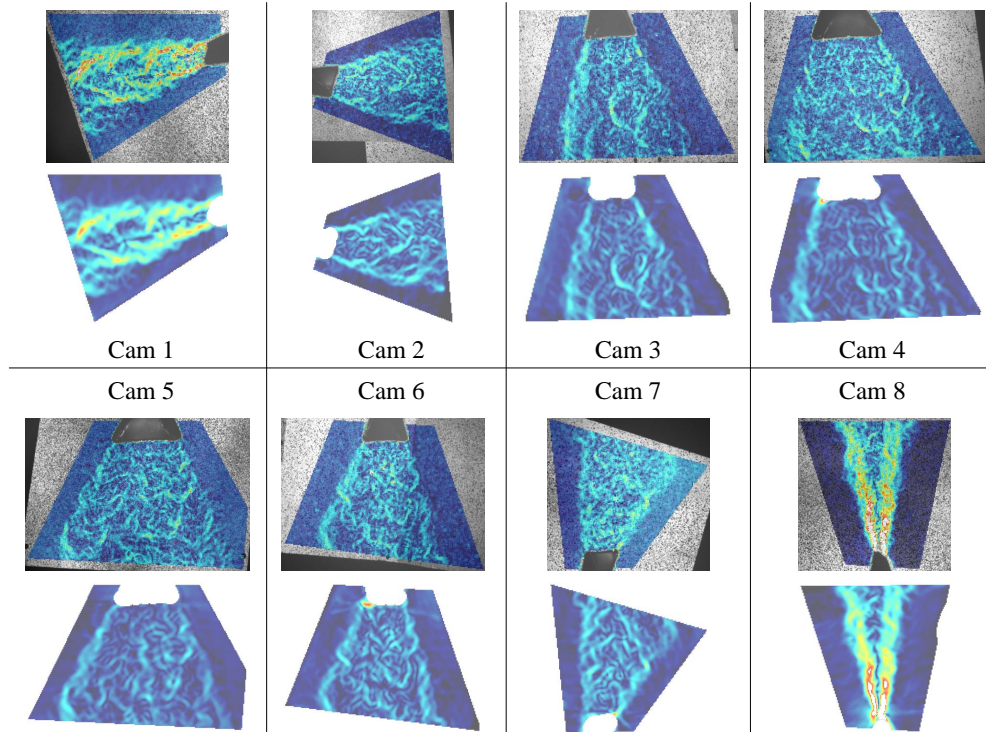
Fig. 16 Flat nozzle heat gun 2D BOS results (top image) and back-projection of the reconstruction (bottom image). Contours are colored by total pixel displacement, and have the same scale for all images.

can be seen as the top images for each camera in Fig. 16, and the projections of the reconstructed volume back to the appropriate camera positions are shown as the bottom images in that figure. The 2D BOS signals for cameras 2 through 7 look weaker than for cameras 1 and 8 because they are viewing the side of the flat nozzle, whereas cameras 1 and 8 are viewing the flat nozzle from the edge. For all the cameras, the projections of the reconstruction match the 2D BOS images well, as they did for the round nozzle data.
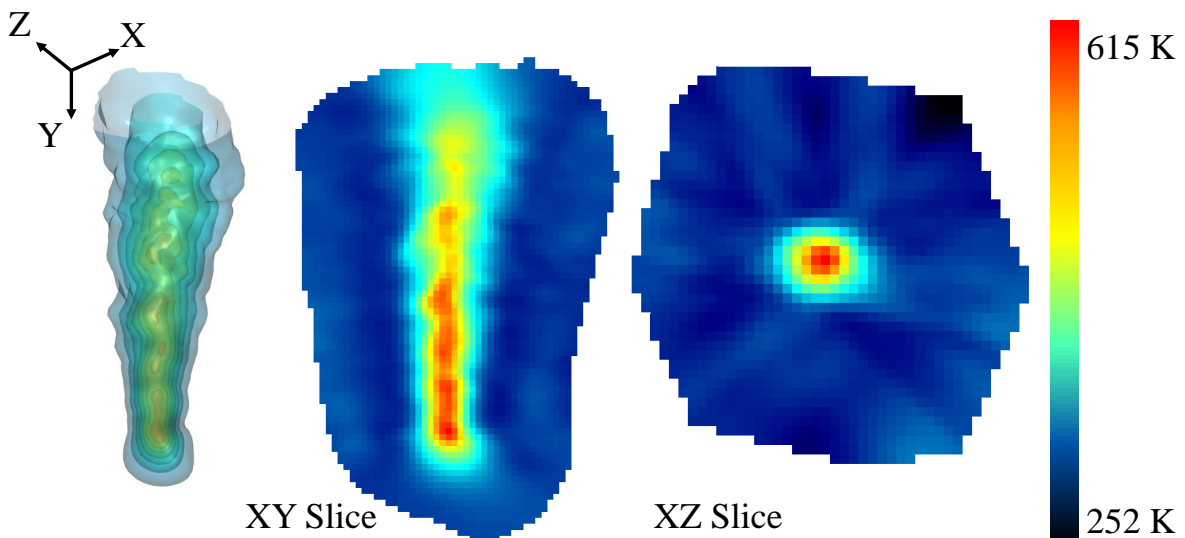

Fig. 17 Round nozzle heat gun tomographic reconstruction (left), with XY (center) and XZ slices (right).
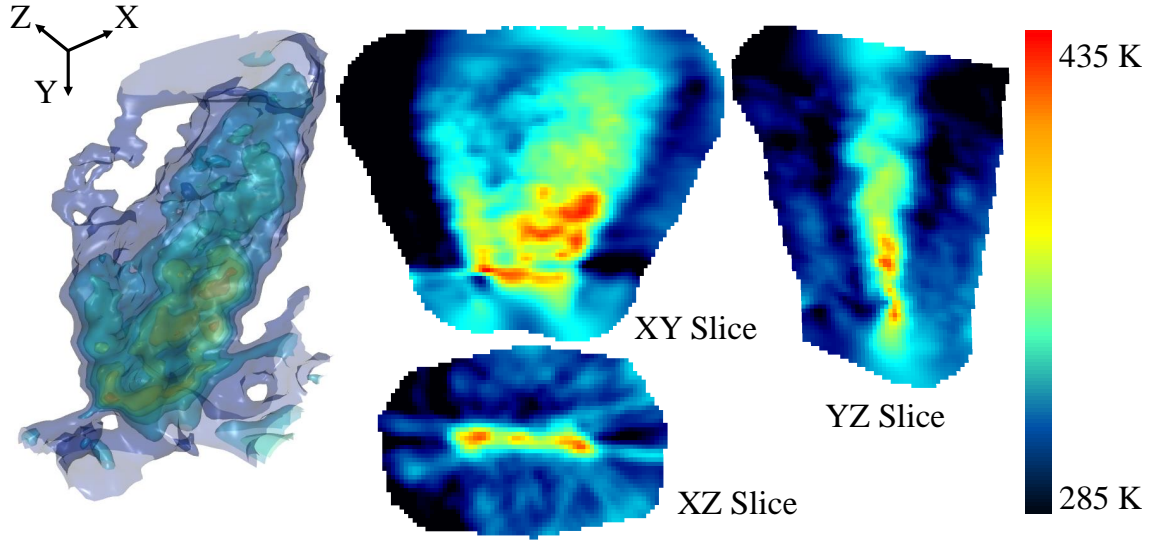
Fig. 18 Flat nozzle heat gun tomographic reconstruction (left), with XY (top center), XZ (bottom center), and YZ slices (right).

Figures 17 and 18 show results of the tomographic reconstruction. Iso-surfaces colored by temperature are shown in the images to the left. Note the different temperature scales for the two figures. The XY slice of Fig. 17 shows typical plume with the hotter air concentrated near the nozzle exit, and cooler air as the plume rises and mixes with the surrounding ambient air. The XZ slice of the same figure shows the round plume exiting from the round nozzle as expected. The temperatures seem reasonable based on typical temperatures in heat guns. The heat gun used in these experiments was not allowed to fully get up to temperature, and was instead turned on a few moments before data acquisition, which could explain the slightly lower temperatures. In Fig. 18, three separate slices are shown since the flow field is no longer axisymmetric. The XY slice shows the flat nozzle from the size, and captures the expansion of the flow out at an angle. In contrast, the YZ slice is narrow, and more closely approximates the XY slice from Fig. 17, although it is important to note that the flat nozzle thickness is smaller than the round nozzle diameter, which accounts for the thinner YZ slice exit plume. The XZ slice shows a cross-sectional view of the exit of the flat nozzle, with high temperatures across its length. The temperatures calculated for the flat nozzle are significantly lower than the round nozzle, which is due in part to the spreading of the plume over a wider surface. Qualitatively, the reconstructions give confidence in the ability of the camera system to be able to measure and calculate 3D BOS fields for larger tunnel facilities. Future testing is necessary to more thoroughly validate the temperature fields.

E. Round-Nozzle Heat Gun at Ames

After the backgrounds were applied to the tunnel walls at the ARC 11-by 11-foot facility, but before the testing campaign had begun, the round nozzle heat gun was used to check the tomographic reconstruction capability, and to compare it to the results from the LaRC mock-up. Based on the results from the mock-up, it was expected that the reconstruction of the plume would succeed, but there were some added difficulties associated with the processing at the facility. Many of the difficulties arise when the tunnel is pumped down and running, but one issue faced when simply taking heat gun data are the baffled slots that break up the continuity of the background. As mentioned in Section II.A, the slots are used to allow air to pass through the walls between the tunnel test section and the plenum. These slots were not permitted to be covered during the testing campaign, and so the background material was cut in size to only be fixed to the solid wall and windows. These slots show up in all frames and must be masked out prior to the tomographic reconstruction to avoid locations with artificially large or small displacements in the 2D BOS data.

The masked 2D BOS images can be seen as the top image for each camera in Fig. 19. Every camera image required masking of the slots, and since these were the final orientations of the cameras for the actual tests, those run images also required the same level of masking. Note that since camera 4 only viewed the edge of the plume due to the positioning of the heat gun out of the FOV, it was excluded from the reconstruction results in this section. The reconstructed
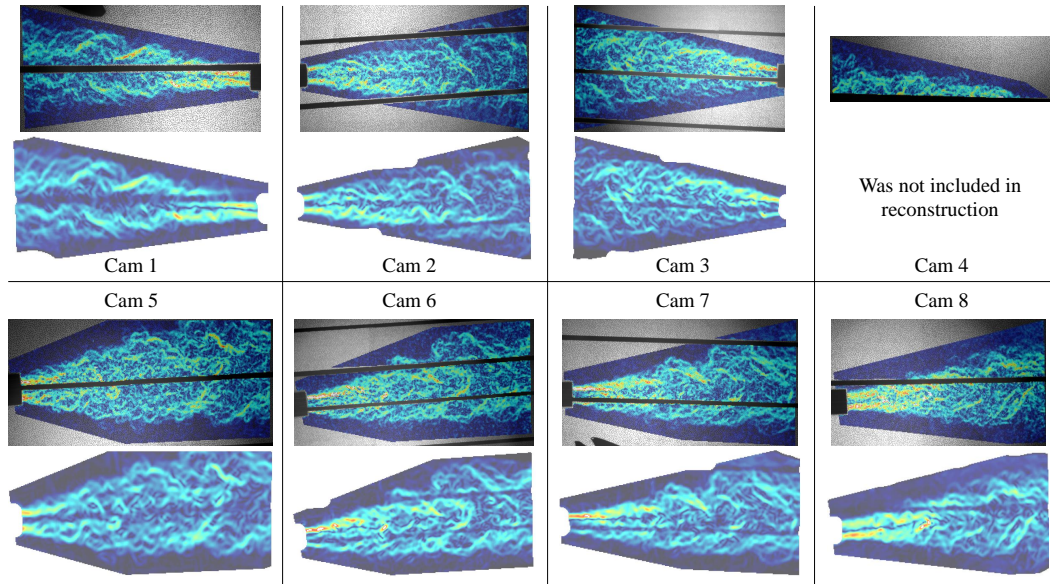
Fig. 19 **Round nozzle heat gun 2D BOS results (top image) and back-projection of the reconstruction (bottom image) from the ARC 11-by- 11-foot tunnel facility. Contours are colored by total pixel displacement, and have the same scale for all images.**
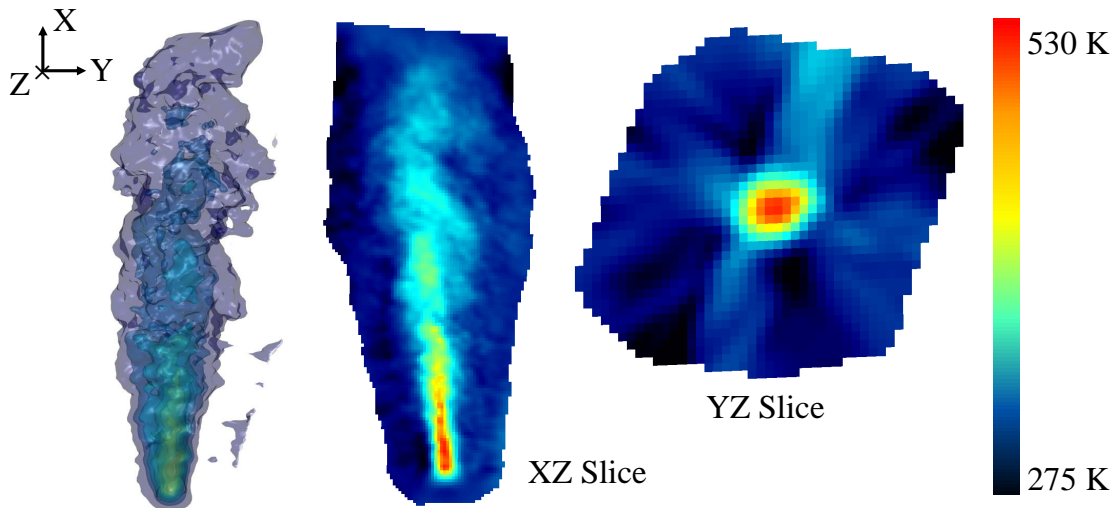

Fig. 20 **ARC round nozzle heat gun tomographic reconstruction (left), with XZ (center) and YZ slices (right).**

back-projections from the tomographic volume to the individual camera positions are shown in the bottom images for each camera in Fig. 19. The flow field structures are very similar to the original 2D BOS results obtained in the LaRC mock-up, and the slots seem to have a minor influence on the reconstruction, appearing as faint regions with little signal. The structures seem to simply jump over the masked slots, which builds confidence for the processing of the actual run data.

A 3D view of the tomographic reconstruction is shown in the left image of Fig. 20, which plots the iso-surfaces of the entire plume from a temperature of 275 K up to a maximum of 530 K. The plume structure seen in the 2D BOS images is evident here, and the slot masking is not visible. In the center and right images of Fig. 20 are the XZ slice and YZ slice of the reconstruction. The XZ slice shows the characteristic plume, with a hot core that decreases in temperature as it mixes with the cooler surrounding air. The YZ slice shows the circular structure of the plume due to

the round nozzle. These reconstruction results give confidence in the tomographic BOS measurements in the ARC wind tunnel facility.

F. Lessons Learned

The experimental setup and measurements discussed in this paper were used in preparation for a test at the ARC 11-by 11-foot Transonic Wind Tunnel, with limited time available for setup, data acquisition, and tear-down. Below is a list of lessons learned (in no particular order) during the LaRC mock-up tests that directly led to a successful testing campaign at the ARC tunnel.

1) The calibration plate must be perfectly flat. This includes making sure it is glued flat to its backing plate and that the plate does not have any curvature. For the large calibration plate size needed for these measurements, the aluminum honeycomb Alumalite was the best option to decrease weight but maintain the necessary rigidity.
2) While not the case in the study by Nicolas *et al.* [42], the calibration plate here must be absolutely steady when taking images. That is, the fiducials must be crisp and clear, without any blur due to small movements of the board during acquisition. Lights external to the camera modules were used to be able to keep the camera exposures low to minimize blur. The calibration plate was also fixed on a mounting system and locked in place for each calibration view.
3) The initial calibration plate fiducial spot sizes were too small and close together. Adjustment of the size and spacing was required in order to get a successful calibration.
4) Longer length wires had been used in the past to connect the LED to the driver circuit, but the total intensity of the output light was lower than the current design. The solution was to entirely remove wires from the system, directly connect the LED to spade connectors attached to the PCB, and the make the traces on the PCB between the power and the LED as short and wide/thick as possible.
5) Using a 50 Ω load resistor on the last of the daisy-chained PCB trigger connections pulled the cameras out of sync. When not using the terminating 50 Ω load resistor, the cameras would fire synchronously. The cause of this is being investigated, but might be due to the relatively low input impedance ($\approx$ 1-2 kΩ) of the pulsing circuit.
6) If the calibration was not successful, a general solution was to add more views at different calibration plate angles and run it again. A method is currently being developed to automate the calibration process with a stepper motor to rotate the calibration plate. This will minimize the calibration target motion caused by manual rotation, and allow the calibration procedure to be performed remotely, which is important for test sections where access is limited.
7) The calibration had a higher chance of success when the calibration plate was oriented more orthogonal to the cameras. At the ARC tunnel, since some cameras were more out-of-plane than others, the stand that the calibration plate was on was rotated such that when the plate was facing that camera, it was as orthogonal to the camera as could be.
8) When the frame rate was set higher in the software (but still below the allowable threshold for each camera), dropped frames occasionally occurred. Although the data did not need to be time-resolved, all eight cameras must be taking data at the exact same time, or the reconstruction would be not possible. To avoid dropped frames, the cameras were run at a lower frame rate (4 Hz) to ensure continuous, reliable acquisition. This was also due in part to the addition of two additional cameras that were used for simultaneous photogrammetry. After testing at ARC was completed, the camera system was able to be run at 10 Hz with seven cameras.

IV. Conclusion

Tomographic background-oriented schlieren measurements were planned at the 11-by 11-foot Transonic Wind Tunnel at NASA Ames Research Center to provide non-intrusive visualization of the flow field around a flight vehicle, and in preparation, a mock-up of the tunnel was constructed at NASA Langley Research Center. A collaborative effort between researchers at NASA's Langley, Glenn, and Ames Research Centers tested the diagnostic system prior to its installation at the tunnel to evaluate the probability of a successful testing campaign.

Camera modules were designed in-house at Langley to provide on-axis LED lighting to maximize the return from the retroreflective backgrounds. A custom data acquisition system was built at Glenn to trigger the cameras and LEDs synchronously for eight cameras located approximately 180° circumferentially around the test section. The cameras

were run at 4 Hz during acquisition, since time-resolved measurements were not required. During the tunnel tests at Ames, two extra cameras were included in the system to obtain simultaneous photogrammetry images. A simple background speckling method using a spray paint can with a drilled out nozzle was used to create the backgrounds for the Langley mock-up, while at Ames, a novel method of printing the speckle onto the background material was developed. Installation of the tomographic BOS system at Langley took place in November 2019, while the tunnel tests took place in early-to-mid December 2019.

A tea light candle and a heat gun with two different nozzle attachments (round and flat) were used to provide an index of refraction gradient field as the BOS signal. The 2D BOS results were first obtained, and using a volume calibration, the tomographic reconstruction was computed. Qualitative observations of the results indicated that good 3D reconstructions were possible with small objects in a large wind tunnel facility. After the system was installed at the Ames tunnel, heat gun data akin to the mock-up system was taken, with similar results obtained, instilling confidence in the installed system for the flight vehicle testing. The design and installation of this system was made possible by the collaborative effort of the three NASA centers, and results from the flight vehicle tests will be presented in a future work.

Acknowledgments

References

[1] Dalziel, S. B., Hughes, G. O., and Sutherland, B. R., "Whole-field density measurements by 'synthetic schlieren'," *Experiments in Fluids*, Vol. 28, No. 4, 2000, pp. 322–335.

[2] Raffel, M., Richard, H., and Meier, G. E. A., "On the applicability of background oriented optical tomography for large scale aerodynamic investigations," *Experiments in Fluids*, Vol. 28, No. 5, 2000, pp. 477–481.

[3] Raffel, M., Tung, C., Richard, H., Yu, Y., and Meier, G. E. A., "Background oriented stereoscopic schlieren (BOSS) for full-scale helicopter vortex characterization," *9th International Symposium on Flow Visualization*, Heriot-Watt University, Edinburgh, 2000.

[4] Richard, H., and Raffel, M., "Principle and applications of the background oriented schlieren (BOS) method," *Measurement Science and Technology*, Vol. 12, No. 9, 2001, pp. 1576–1585.

[5] Settles, G. S., *Schlieren and Shadowgraph Techniques*, 1st ed., Springer Berlin Heidelberg, 2006.

[6] Raffel, M., "Background-oriented schlieren (BOS) techniques," *Experiments in Fluids*, Vol. 56, No. 3, 2015.

[7] Micol, J. R., "Langley Aerothermodynamic Facilities Complex: Enhancements and Testing Capabilities," *36th AIAA Aerospace Sciences Meeting and Exhibit*, American Institute of Aeronautics and Astronautics, 1997.

[8] Berger, K., Rufer, S., Hollingsworth, K., and Wright, S., "NASA Langley Aerothermodynamics Laboratory: Hypersonic Testing Capabilities," *53rd AIAA Aerospace Sciences Meeting*, American Institute of Aeronautics and Astronautics, 2015.

[9] Erickson, G. E., "Overview of Supersonic Aerodynamics Measurement Techniques in the NASA Langley Unitary Plan Wind Tunnel," Tech. rep., NASA Langley Research Center, 2007.

[10] Kmak, F. J., "Modernization and activation of the NASA Ames 11- by 11-Foot Transonic Wind Tunnel," *21st Aerodynamic Measurement Technology and Ground Testing Conference*, American Institute of Aeronautics and Astronautics, 2000.

[11] Corlett, W. A., "Operational Flow Visualization Techniques in the Langley Unitary Plan Wind Tunnel," Tech. rep., NASA Langley Research Center, 1982.

[12] II, T. J. G., Baerny, J. K., and Ross, J. C., "Wind Tunnel Flow Field Visualizations of the Space Launch System Vehicle Ascent," *AIAA Aviation 2019 Forum*, 2019.

[13] Winski, C. S., Danehy, P. M., Watkins, A. N., Shea, P. R., Meeroff, J. G., Lowe, K. T., and Houlden, H. P., "Space Launch System Booster Separation Supersonic Powered Testing with Surface and Off-body Measurements," *AIAA Aviation 2019 Forum*, 2019.

[14] Atcheson, B., Ihrke, I., Heidrich, W., Tevs, A., Bradley, D., Magnor, M., and Seidel, H.-P., "Time-resolved 3D Capture of Non-stationary Gas Flows," *ACM Transactions on Graphics*, Vol. 27, No. 5, 2008, p. 1.

[15] Grauer, S. J., Unterberger, A., Rittler, A., Daun, K. J., Kempf, A. M., and Mohri, K., "Instantaneous 3D flame imaging by background-oriented schlieren tomography," *Combustion and Flame*, Vol. 196, 2018, pp. 284–299.

[16] Zhang, L., Song, Y., Qu, X., Li, Z., and He, A., "Quantitative reconstruction of 3D flow density fields by a direct computerized tomography method of BOS," *Optical Metrology and Inspection for Industrial Applications V*, edited by S. Han, T. Yoshizawa, and S. Zhang, SPIE, 2018.

[17] Bathel, B. F., Weisberger, J. M., and Jones, S. B., "Development of Tomographic Background-Oriented Schlieren Capability at NASA Langley Research Center," *AIAA Aviation 2019 Forum*, 2019.

[18] Liu, H., Sun, B., and Cai, W., "kHz-rate volumetric flame imaging using a single camera," *Optics Communications*, Vol. 437, 2019, pp. 33–43.

[19] Liu, H., Shui, C., and Cai, W., "Time-resolved three-dimensional imaging of flame refractive index via endoscopic background-oriented Schlieren tomography using one single camera," *Aerospace Science and Technology*, Vol. 97, 2020, p. 105621.

[20] Zeb, M. F., Ota, M., and Maeno, K., "Quantitative Measurement of Heat Flow in Natural Heat Convection Using Color-Stripe Background Oriented Schlieren (CSBOS) Method," *Journal of the Japanese Society for Experimental Mechanics*, Vol. 11, 2011, pp. 141–146.

[21] Hartmann, U., Adamczuk, R., and Seume, J. R., "Tomographic Background Oriented Schlieren Applications for Turbomachinery," *53rd AIAA Aerospace Sciences Meeting*, American Institute of Aeronautics and Astronautics, 2015.

[22] Venkatakrishnan, L., and Suriyanarayanan, P., "Density field of supersonic separated flow past an afterbody nozzle using tomographic reconstruction of BOS data," *Experiments in Fluids*, Vol. 47, No. 3, 2009, pp. 463–473.

[23] Todoroff, V., Plyer, A., Besnerais, G. L., Champagnat, F., Donjat, D., Micheli, F., and Millan, P., "3D Reconstruction of the Density Field of a Jet using Synthetic BOS Images," *15th International Symposium on Flow Visualization*, 2012.

[24] Adamczuk, R. R., Hartmann, U., and Seume, J., "Experimental demonstration of Analyzing an Engine's Exhaust Jet with the Background-Oriented Schlieren Method," *AIAA Ground Testing Conference*, American Institute of Aeronautics and Astronautics, 2013.

[25] Todoroff, V., Besnerais, G. L., Donjat, D., Micheli, F., Plyer, A., and Champagnat, F., "Reconstruction of instantaneous 3D flow density fields by a new direct regularized 3DBOS method," *17th International Symposium on Applications of Laser Techniques to Fluid Mechanics*, 2014.

[26] Donjat, D., Nicolas, F., Plyer, A., Micheli, F., Cornic, P., Besnerais, G. L., Champagnat, F., Sant, Y. L., and Deluc, J.-M., "Study of a co-flowing hot jet: an application of direct 3DBOS technique in research wind tunnel," *10th Pacific Symposium on Flow Visualization and Image Processing*, 2015.

[27] Hartmann, U., and Seume, J. R., "Combining ART and FBP for improved fidelity of tomographic BOS," *Measurement Science and Technology*, Vol. 27, No. 9, 2016, p. 097001.

[28] Lang, H. M., Oberleithner, K., Paschereit, C. O., and Sieber, M., "Measurement of the fluctuating temperature field in a heated swirling jet with BOS tomography," *Experiments in Fluids*, Vol. 58, No. 7, 2017.

[29] Nicolas, F., Donjat, D., Plyer, A., Champagnat, F., Besnerais, G. L., Micheli, F., Cornic, P., Sant, Y. L., and Deluc, J. M., "Experimental study of a co-flowing jet in ONERA's F2 research wind tunnel by 3D background oriented schlieren," *Measurement Science and Technology*, Vol. 28, No. 8, 2017, p. 085302.

[30] Amjad, S., Soria, J., and Atkinson, C., "Time-Averaged Three-Dimensional Density and Temperature Field Measurement of a Turbulent Heated Jet Using Background-Oriented Schlieren," *21st Australasian Fluid Mechanics Conference*, 2018.

[31] Nicolas, F., Donjat, D., Micheli, F., Besnerais, G. L., Plyer, A., Cornic, P., Champagnat, F., and Michou, Y., "Experimental study of a counter-flow jet in ONERA's S1MA wind tunnel by 3D background oriented schlieren," *18th International Symposium on Flow Visualization*, Zurich, Switzerland, 2018. 18th International Symposium on Flow Visualization.

[32] Ota, M., Hamada, K., Kato, H., and Maeno, K., "Computed-tomographic density measurement of supersonic flow field by colored-grid background oriented schlieren (CGBOS) technique," *Measurement Science and Technology*, Vol. 22, No. 10, 2011, p. 104011.

[33] Sourgen, F., Leopold, F., and Klatt, D., "Reconstruction of the density field using the Colored Background Oriented Schlieren Technique (CBOS)," *Optics and Lasers in Engineering*, Vol. 50, 2012, pp. 29–38.

[34] Leopold, F., Ota, M., Klatt, D., and Maeno, K., "Reconstruction of the Unsteady Supersonic Flow around a Spike Using the Colored Background Oriented Schlieren Technique," *Journal of Flow Control, Measurement & Visualization*, Vol. 1, 2013, pp. 69–76.

[35] Nicolas, F., Donjat, D., Léon, O., Besnerais, G. L., Champagnat, F., and Micheli, F., "3D reconstruction of a compressible flow by synchronized multi-camera BOS," *Experiments in Fluids*, Vol. 58, No. 5, 2017.

[36] Meyer, T. R., Halls, B. R., Jiang, N., Slipchenko, M. N., Roy, S., and Gord, J. R., "High-speed, three-dimensional tomographic laser-induced incandescence imaging of soot volume fraction in turbulent flames," *Optics Express*, Vol. 24, No. 26, 2016.

[37] Halls, B. R., Hsu, P. S., Jiang, N., Legge, E. S., Felver, J. J., Slipchenko, M. N., Roy, S., Meyer, T. R., and Gord, J. R., "kHz-rate four-dimensional fluorescence tomography using an ultraviolet-tunable narrowband burst-mode optical parametric oscillator," *Optica*, Vol. 4, No. 8, 2017, p. 897.

[38] Raffel, M., Willert, C. E., Scarano, F., Kähler, C., Wereley, S. T., and Kompenhans, J., *Particle Image Velocimetry*, Springer-Verlag GmbH, 2018.

[39] Lucas, B. D., and Kanade, T., "An Iterative Image Registration Technique with an Application to Stereo Vision," *7th International Joint Conference on Artificial Intelligence*, 1981, pp. 674–679.

[40] Horn, B. K. P., and Shunck, B. G., "Determining Optical Flow," *Artificial Intelligence*, Vol. 17, No. 1, 1981, pp. 185–203.

[41] Smith, N. T., Heineck, J. T., and Schairer, E. T., "Optical Flow for Flight and Wind Tunnel Background Oriented Schlieren Imaging," *55th AIAA Aerospace Sciences Meeting*, 2017.

[42] Nicolas, F., Todoroff, V., Plyer, A., Besnerais, G. L., Donjat, D., Micheli, F., Champagnat, F., Cornic, P., and Sant, Y. L., "A direct approach for instantaneous 3D density field reconstruction from background-oriented schlieren (BOS) measurements," *Experiments in Fluids*, Vol. 57, No. 13, 2016.

[43] Grauer, S. J., and Steinberg, A. M., "Fast and robust volumetric refractive index measurement by unified background-oriented schlieren tomography," *Experiments in Fluids*, Vol. 61, No. 3, 2020, p. 80.

[44] Schairer, E. T., Heineck, J. T., Walker, S. M., and Yaste, D. M., "Predicting Camera Views for Image-Based Measurements in Wind Tunnels," *43rd AIAA Aerospace Sciences Meeting and Exhibit*, American Institute of Aeronautics and Astronautics, 2005.

[45] Kushner, L. K., and Schairer, E. T., "Planning Image-Based Measurements in Wind Tunnels by Virtual Imaging," *49th AIAA Aerospace Sciences Meeting including the New Horizons Forum and Aerospace Exposition*, American Institute of Aeronautics and Astronautics, 2011.

[46] Burgess, G., Shortis, M. R., and Scott, P., "Photographic assessment of retroreflective film properties," *ISPRS Journal of Photogrammetry and Remote Sensing*, Vol. 66, No. 5, 2011, pp. 743–750.